Research trends on minimizing the size of noble metal catalysts for Li-CO₂ batteries: From nanoparticle to single atom

Yeo-Jin Rho, Yoon Jeong Yoo, and Won-Hee Ryu[†]

Department of Chemical and Biological Engineering, Sookmyung Women's University,
100 Cheongpa-ro 47-gil, Yongsan-gu, Seoul 04310, Korea

Abstract−Li-CO₂ batteries involve a spontaneous conversion reaction by injecting CO_2 into a cathode, and reversibly store energy without additional energy input through a charging and discharging process, thereby achieving carbon neutrality. Noble metal-based electrocatalysts have been actively considered to efficiently facilitate the Li-CO₂ reaction with reduced overvoltage, yet the use of expensive noble metal catalysts is a barrier to developing this type of Li-CO₂ battery. Here, the importance of minimizing the size of noble metal particle-based catalysts for Li-CO₂ batteries is reviewed and emphasized. Comparisons of the performance of Li-CO₂ cells with noble metal catalysts, such as Ru and Ir, showed that overpotential is lower when particle sizes are reduced to the single atom-scale. This indicates that the smaller the particle-to-atomic scale, the greater the catalytic activity. Recent diverse studies based on nano- or atomic-scale Ru and Ir catalysts affecting catalytic activities of the Li-CO₂ cell reaction are introduced. Other single atom catalyst candidates are also suggested for Li-CO₂ battery applications.

Keywords: Noble Metal, Single Atom Catalyst, Nanoparticle, Li-CO₂ Battery, Carbon Capture and Storage

INTRODUCTION

With accelerated industrial growth, the concentration of CO_2, which is a primary greenhouse gas, has rapidly increased in the atmosphere, causing severe global warming and climate change issues [1-5]. To address this global challenge, carbon capture and storage (CCS) technologies are a promising methods of accomplishing a meaningful reduction in CO_2 emissions in the near-term [6-8]. Although there are typically numerous technical options (e.g., amine-based absorbents) that are suitable for CCS activity, the challenges associated with excess energy and cost consumption in terms of scaling up need to be tackled [9-11].

Li-CO₂ batteries have emerged as a reliable CCS candidate operating in an electrochemical manner, dealing with economical limitations of existing CCS systems [12-15]. Using a reversible electrochemical CCS method, Li-CO₂ cells are capable of spontaneous energy storage and simultaneous environmental CO_2 fixation without external electricity [16]. Generally, Li-CO₂ batteries consist of Li metal for anodes, non-aqueous electrolytes, ionic conductive separators, and porous air cathodes in which CO_2 gas flows into the electrode [17-19]. Through charging and discharging reactions, the cathode engages in the absorption and release of CO_2 gas on the air electrode, accompanied with a conversion reaction with Li ions [20]. During the discharge reaction, CO_2 reduction ($4Li^+ + 3CO_2 + 4e^- \rightarrow 2Li_2CO_3 + C$, $-0.24\ V_{SHE}$) occurs spontaneously in combination with the counter anodic reaction of Li ($Li \rightarrow Li^+ + e^-$, $-3.04\ V_{SHE}$) [16,17,21-24]. Based on this redox chemistry of CO_2 in the Li-CO₂

system, a high cell voltage (~2.8 V) and theoretical specific energy density ($1{,}876\ \mathrm{W\ h\ kg^{-1}}$) can be achieved [25]. Therefore, the Li-CO₂ battery system is a promising candidate to realize carbon neutrality by storing substantial energy. Despite their potential for simultaneous CCS and electrochemical energy storage, critical interferences such unsuitable battery life and low efficiency are often found [26-28]. One of the disturbances of the Li-CO₂ reaction is the irreversible electrochemical decomposition of insulating Li_2CO_3 products that are yielded during recharging [29]. In general, Li_2CO_3 has a wide bandgap that exhibits high thermodynamic stability; thus, an excessive potential bias is usually required for the decomposition of Li_2CO_3 (>4.3 V vs. Li/Li^+) [22-24]. Inherent properties of the Li_2CO_3 products therefore tend to induce large overpotential and slower reaction kinetics in the Li-CO₂ cell, thereby deteriorating the lifespan of the battery [13].

To overcome the limitations of the Li-CO₂ battery, it is necessary to introduce highly active and conductive electrocatalysts [30-32]. Electrocatalysts applied to the air electrode have been extensively studied because Li-CO₂ batteries usually depend on the cathodes with CO_2 reduction and evolution reaction catalytic activity [16, 33-36]. Various types of electrocatalysts controlling chemical composition, morphology, and size have been considered for Li-CO₂ batteries [15,20,37-39]. Among these studies, noble metal-based catalysts, especially Ru and Ir, have received a considerable amount of attention for their excellent activity, selectivity, and stability, and they have been widely used in environmental protection and new energy fields, including in Li-CO₂ batteries [40-49]. The intrinsic state of semi-filled antibonding of precious metal catalysts creates suitable binding energy between the catalysts and reactants, which advances the reaction kinetics [50-54]. Thus, it is well-known that precious metal catalysts have superior catalytic activity for CO_2 reduction and

precipitation reactions; however, the high cost and low abundancy of noble metal elements are decisive and practical limitations for scaling to an industrial level [55-60]. For this reason, overcoming the economic issues of noble metal catalysts is important for the development of the overall electrochemical industry as well as battery fields [61-65].

Up to now, it has been spotlighted that size control of noble metal catalyst particles is crucial for determining the performance of Li-CO_2 batteries and can reduce the burden of cost [34,66,67]. In most recent studies, the smaller the catalyst particle size from the nanoparticle to atomic scale, the more active the electron transfer of the catalytic active sites [68-73]. By eventually minimizing the size of the catalyst particles to a single atomic unit, various positive changes, such as high catalytic activity and selectivity toward the Li-CO_2 reaction, can be achieved [74-78]. Single atom catalysts (SACs) involve catalytically active individual and distinctive metal atoms anchored to supports, and these can display desirable metal utilization with maximized reaction surfaces exposed to reactants as well as allow facile catalytic reactions [75,79]. The interaction between individual atoms and supports as well as the unsaturated coordination environments of the SACs can improve electrocatalytic performance, resulting in tunable electronic structures [74,80-83].

In this short review, a series of various particle sizes of noble metal-based electrocatalysts, including Ru and Ir, are looked at, and how the size effect determines the performance of the catalytic reaction is explained through comparison of the overpotentials of Li-CO_2 cells. This review contributes to current knowledge of noble metal-based electrocatalysts freshly applied to Li-CO_2 cells and informs on the importance of controlling the electrocatalyst particle size towards the atomic scale. We believe that introduction of SACs accomplishes dual goals of maximizing catalytic activities and minimizing usage of noble metals (Fig. 1).

Ru PARTICLE-BASED ELECTROCATALYSTS

Ru, a precious metal catalyst with broad functions, exhibits out-standing catalytic activity in electrochemical reactions, including a reversible reaction of Li-CO_2 [84-87]. Here, representative studies on the catalytic efficiency of Ru electrocatalysts according to particle size (from nanoparticle-to-single atom size) are compared.

1. Morphology and Ru Particle Size Characterization

Diverse size ranges of Ru catalysts have been loaded on to various carbon supports, and representative examples are shown in Fig. 2. Qian et al. introduced Ru nanoparticles loaded on carbon nanofiber (Ru/CNF) (Fig. 2(a)) [41]. The average diameter of Ru particles is 9.0±2.5 nm. Yang et al. reported Ru nanoparticles supported on Super P carbon (Ru/Super P) catalyst by facile heat treatment and the magnetron sputtering method (Fig. 2(b)) [88]. Metallic Ru nanoparticles were homogeneously loaded on Super P and the particle size was estimated to be about 5-10 nm. As shown in Fig. 2(a), Qian et al. also synthesized activated CNF (ACNF) substrates (Fig. 2(c)) [41]. ACNF is formed after subsequent gasification treatment of CNF under a CO_2 atmosphere, and Ru particles are mounted on both CNF and ACNF by the thermal shock method (Ru/ACNF). The average diameter of Ru particles is 4.1±0.9 nm for Ru/ACNF. Qiao et al. synthesized Ru nanoparticles dispersed on N and S co-doped graphene nanosheets (Ru/NS-G) by ultrasonication and a hydrothermal procedure (Fig. 2(d)) [89]. The hexagonal Ru nanoparticles were uniformly distributed on NS-G supports with a mean size of 2.6±0.6 nm. TEM observations of smaller Ru particles were conducted in some studies (Fig. 2(e), (f)) [18,90]. As seen in Fig. 2(e), RuO_2 nanoparticles with diameters of around 2 nm were evenly loaded on to carbon nanotubes ranging in size from 10 to 30 nm (RuO_2/CNT) through a series of annealing processes. Similarly, Ru nanoparticles with an average size of 2 nm were functionalized on wrinkled graphene nanosheets (Ru/G) (Fig. 2(f)). To further minimize Ru catalyst size beyond the nanoscale level, Ru SACs were recently introduced for Li-CO_2 batteries [91,92]. Contrary to the catalyst nanoparticles, numerous bright and tiny dots, which are Ru atoms, are homogeneously dispersed on the substrates (Fig. 2(g), (h)). As shown in Fig. 2(g), Ru atoms, which are marked with red circles, are loaded on to a Co_3O_4 nanosheet surface supported on a
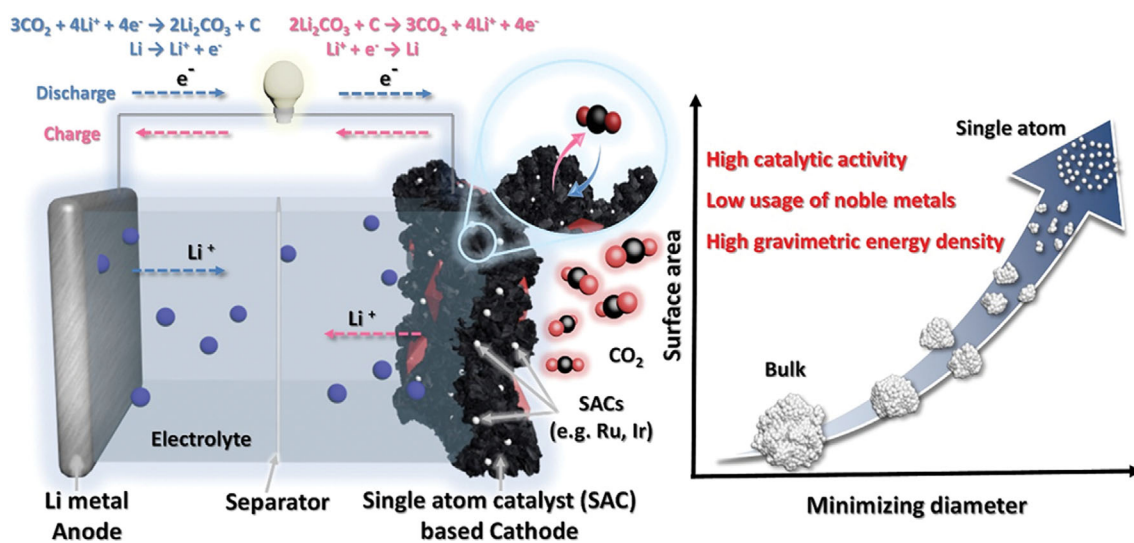

Fig. 1. Schematic illustration of the size effect of noble metal particle-based catalysts.
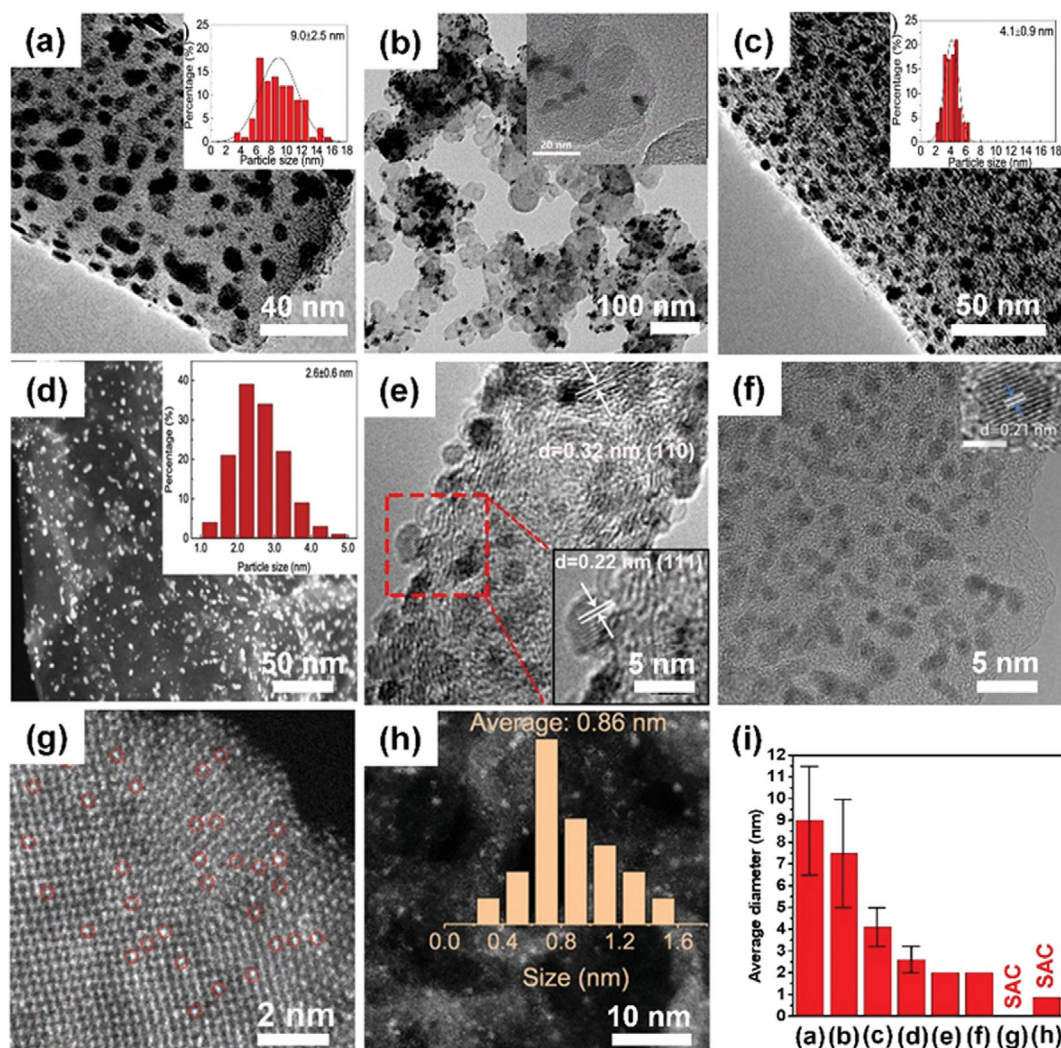
Fig. 2. (a)-(f) TEM images, (g), (h), HAADF-STEM images, and (i) Size distribution graph of (a) Ru/CNF (reproduced with permission from ref. [41], copyright 2019, Royal Society of Chemistry), (b) Ru/Super P (reproduced with permission from ref.[88], copyright 2017, Royal Society of Chemistry), (c) Ru/ACNF (reproduced with permission from ref. [41], copyright 2019, Royal Society of Chemistry), (d) Ru/NS-G (reproduced with permission from ref. [89], copyright 2020, Elsevier B.V.), (e) RuO$_2$/CNT (reproduced with permission from ref. [90], copyright 2019, American Chemical Society), (f) Ru/G (reproduced with permission from ref. [18], copyright 2017, American Chemical Society), (g) Ru SAC/Co$_3$O$_4$-CC (reproduced with permission from ref. [91], copyright 2021, John Wiley and Sons), (h) Ru SAC/NCB (reproduced with permission from ref. [92], copyright 2022, John Wiley and Sons).

carbon cloth (Ru/CO$_3$O$_4$-CC). Fig. 2(h) shows Ru single atoms dispersed on N-doped carbon nanobox supports (Ru SAC/NCB). The average diameter of Ru SACs is about 0.86 nm. As with the previous materials, both Ru SACs are synthesized through facile calcination. The average size distribution of Ru particle-based catalysts is summarized in Fig. 2(i). The average diameter was miniaturized from 9.0 nm for Ru/CNF (Fig. 2(a)) to 0.86 nm for Ru SAC/NCB (Fig. 2(h)).

2. Electrochemical Performance of Ru Particle-based Catalysts Embedded in Li-CO$_2$ Cells

Based on the size information of Ru nanoparticle catalysts or SACs (Fig. 2), the electrochemical performance of diverse Ru-based catalysts in Li-CO$_2$ cells is shown in Fig. 3. Profiles were organized and compared in order from large to small Ru particle sizes, from nanoparticle to single atom. We compared the catalytic activity among the SAC materials mainly via overvoltage comparison, where the overvoltage means the difference between the voltage plateau generated for discharge and following charge processes. In Fig. 3(a), the charge/discharge curves of the Ru/CNF cathode, which has the largest average diameter (9.0±2.5 nm) of Ru particles, and the Ru/ACNF cathode (4.1±0.9 nm) are shown at a current density of 100 mA g^{-1} with a limiting capacity of 500 mAh g^{-1} in Li-CO$_2$ batteries [41]. The Ru/CNF exhibits a large overpotential of 1.79 V with terminal discharge and charge voltages of 2.51 and 4.3 V, respectively. However, for the Ru/ACNF, which has smaller and more dispersed particles than Ru/CNF, the discharge and charge plateau voltages are 2.8 and 4.15 V, respectively, indicating 1.35 V of overpotential. Compared with the Ru/CNF, the Ru/ACNF exhibits lower overpotential in Li-CO$_2$ cells. After 50 cycles, the charge and discharge terminal voltage of Ru/ACNF remains at about 1.43 V. More-
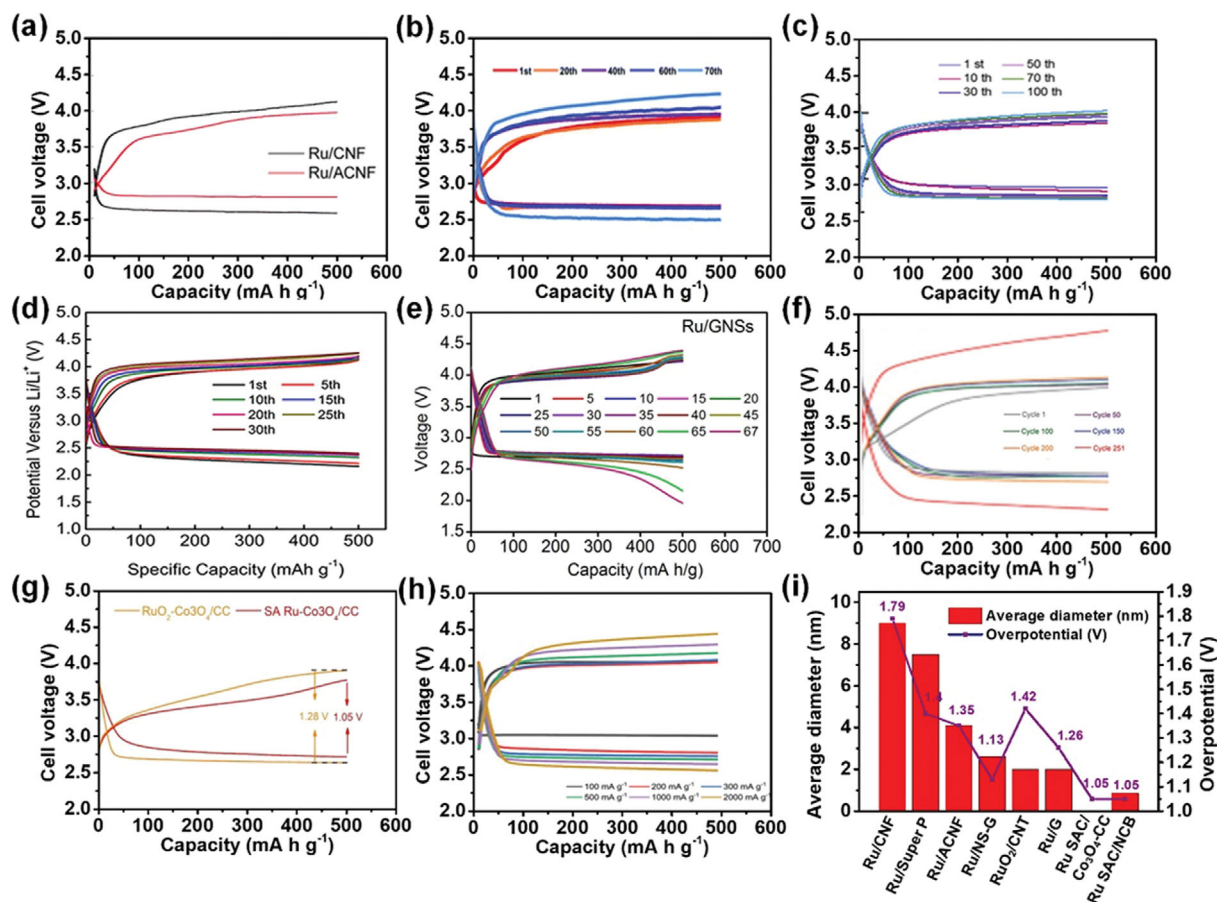
Fig. 3. Electrochemical performance in Li-CO$_2$ batteries. (a)-(h) Charge/discharge profiles, (i) average diameters, and overpotentials comparison of (a) Ru/CNF and Ru/ACNF (reproduced with permission from ref. [41], copyright 2019, Royal Society of Chemistry), (b) Ru/Super P (reproduced with permission from ref. [88], copyright 2017, Royal Society of Chemistry), (c) Ru/NS-G (reproduced with permission from ref. [89], copyright 2020, Elsevier B.V.), (d) RuO$_2$/CNT (reproduced with permission from ref. [90], copyright 2019, American Chemical Society), (e) Ru/G (reproduced with permission from ref. [18], copyright 2017, American Chemical Society), (f) Ru SAC/Co$_3$O$_4$-CC, (g) RuO$_2$/Co$_3$O$_4$-CC (reproduced with permission from ref. [91], copyright 2021, John Wiley and Sons), and (h) Ru SAC/NCB (reproduced with permission from ref. [92], copyright 2022, John Wiley and Sons) at a current density of 100 mA g^{-1} with a limiting capacity of 500 mAh g^{-1}.

over, at different current densities of 800 and 1,000 mA g^{-1}, the overpotentials of Ru/ANCF are 1.79 and 1.81 V, respectively. The full discharge and charge profiles of Ru/ACNF were also checked, and found to display a discharge plateau at about 2.72 V with 11,495 mAh g^{-1} of capacity. During charging, the reversible charge capacity is 10,715 mAh g^{-1}, corresponding to the recharge voltage of 4.5 V. In summary, the overpotential of two catalysts tested in the same experimental environment can be examined to determine the lowering overpotential that can be realized with miniaturization of Ru noble metal particles by simply changing a support.

In addition to Ru/CNF and Ru/ACNF, there are other Ru-based catalysts for comparing cell performance (Fig. 3(b)-(g)). The discharge and charge curves corresponding to a current density of 100 mA g^{-1} of the Ru/Super P cathode (5-10 nm), in which the Ru particles loaded are smaller than those in the Ru/CNF and larger than those in the Ru/ACNF, are shown in Fig. 3(b) [88]. These data show that the cut-off capacity is 500 mAh g^{-1}, and cycling performance is displayed until the 70th cycle. The discharge and charge

terminal voltages are 2.6 and 4.0 V, respectively, corresponding to an overpotential of 1.4 V, which is lower than that of the Ru/CNF but higher than that of the Ru/ACNF. Regarding the discharge process, the Ru/Super P cathode presents a capacity of 8,229 mAh g^{-1} with a discharge plateau of around 2.54 V. The charging capacity is 7,093 mAh g^{-1}, which corresponds to a charge plateau of 4.25 V. Compared to the Ru/ACNF, which has smaller Ru particles, the full discharge and charge measurements show a worse value for Ru/Super P. The discharge and charge cycle performance of the Ru/NS-G cathode (2.6±0.6 nm) until the 100th cycle is shown in Fig. 3(c) at a current density of 100 mA g^{-1} with a limited specific capacity of 500 mAh g^{-1} [89]. The discharge and charge plateaus are 2.91 and 4.04 V, respectively, and the overpotential is 1.13 V, which is lower than that of the Ru/CNF, Ru/Super P, and Ru/ACNF. After 50 cycles, the overpotential of the Ru/NS-G slightly increases to 1.33 and 1.40 V after 100 cycles; however, this is still lower than that of the Ru/ACNF (1.43 V). In terms of stability, charge/discharge polarization was quite large in 70 cycles in the Ru/super P with

larger particles, but the Ru/NS-G maintained a stable charge/discharge curve for up to 100 cycles. The full discharge and charge profiles individually demonstrate 12,448 and 10,660 mAh g^{-1}, respectively, resulting in a discharge platform of around 2.68 V, which is superior to the Ru/CNF, Ru/Super P, and Ru/ACNF. Additionally, the overpotentials at different current densities, 200, 300, 400, and 500 mA g^{-1}, are 1.14, 1.31, 1.55, and 1.69 V, respectively, and these values are reasonable compared to those of larger Ru particle-based catalysts. In addition to the materials mentioned above, the cell performance after applying catalysts with smaller Ru particles (2 nm), labeled RuO$_2$/CNT and Ru/G at 500 mAh g^{-1} of limited specific capacity, is shown in Fig. 3(d) and (e) [18,90]. The average charge voltages of RuO$_2$/CNT-applied Li-CO$_2$ cells are 3.86, 3.88, and 3.92 V at a current density of 50, 100, and 150 mA g^{-1}, respectively, and the overpotential at 100 mA g^{-1} is 1.42 V, displaying a slightly high value compared to the other cathode materials mentioned in Fig. 3(a)-(c). The full discharge and charge capacities at 50 mA g^{-1} are both 2,187 mAh g^{-1}, corresponding to average discharge and charge plateaus at 2.46 and 3.97 V, respectively. For Ru/G shown in Fig. 3(e), the cell performance tests were conducted under an O$_2$-assisted Li-CO$_2$ battery environment at a current density of 160 mA cm^{-2} showing 67 cycles of cycle stability. The full discharge and charge profiles were conducted at a current density of 80 and 160 mA cm^{-2}. At 80 mA cm^{-2}, the discharge capacity was 4,742 mAh g^{-1}, corresponding to 2.76 V of discharge plateau. For the recharge process, the charge capacity was 4,230 mAh g^{-1}, with 4.02 V of charge plateau, indicating 1.26 V of overpotential. At a higher current density of 160 mA cm^{-2}, the discharge case showed 3,865 mAh g^{-1} of capacity and 2.67 V of plateau. The recharge capacity also showed 3,000 mAh g^{-1} and 4.10 V of terminal voltage. In summary of Fig. 3(a)-(e), the overpotential between discharge and charge at 100 mA g^{-1} of current density was over 1.1 V, displaying 1.13 V of minimum and 1.79 V of maximum. Furthermore, the overpotential tended to fall with decreasing size of the Ru particles and tended to rise again at a larger Ru particle diameter of 2 nm.

To prove the effects of minimizing catalyst size toward SACs, the Li-CO$_2$ cell performance of SACs is shown in Fig. 3(f) and (h). The cell tests of Ru SAC/Co$_3$O$_4$-CC were conducted under a constant current density of 100 mA g^{-1} with a cut-off capacity of 500 mAh g^{-1} (Fig. 3(f)) [91]. The overpotential was a very low value of 1.05 V, indicating excellent catalytic activity. In addition, the overpotential at higher current densities of 200 and 300 mA g^{-1} remained at the lower level compared to those of the Ru nanoparticle-based catalysts above, showing 1.27 and 1.45 V, respectively. In the full discharge and charge process, the full discharge capacity was higher than that of nanoparticle catalysts, showing up to 30,915 and 16,510 mAh g^{-1} at a current density of 100 and 300 mA g^{-1}, respectively. The cycling stability also properly lasted for 251 cycles (2,000 h) with a discharge and charge depth of 800 mAh g^{-1} and current density of 200 mA g^{-1}. Furthermore, in a study performed by Lian et al., an additional test for larger Ru particle catalysts with the same support material was conducted (Fig. 3(g)). The data showed an overpotential of 1.28 V and full discharge capacity of 23,633 mA g^{-1} at 100 mA g^{-1}, which meant poorer catalytic performance than Ru SAC/Co$_3$O$_4$-CC. The test of the Ru SAC/NCB, which is the other Ru SAC in the study, was conducted at diverse current den-

sities with a limiting capacity of 500 mAh g^{-1} (Fig. 3(h)). The discharge plateaus were 3.01, 2.77, 2.73, 2.68, 2.58, and 2.41 V, resulting in overpotentials of 1.05, 1.23, 1.33, 1.47, 1.65, and 1.86 V at 100, 200, 300, 500, 1,000, and 2,000 mA^{-1}, respectively. Compared to the data provided in Fig. 3(a)-(e), this information implies superior catalytic activity of Ru SAC. The full discharge capacity (10,652 mAh g^{-1}) is almost the same as that of other Ru nanoparticle-based catalysts. The size and overpotential summary of the Ru catalysts mentioned above are shown in Fig. 3(i). As Ru size decreased, the overvoltage also decreased. While the overpotential of Ru catalysts with a diameter of 2 nm seemed to slightly increase, the Ru SACs with smaller diameter showed the excellent activity. That is, the results imply that the catalytic activity can be accelerated by atomically reducing the size of the precious metal catalysts. The catalytic reaction can be facilitated by maximizing catalytic reaction sites and their exposed surface.

In summary of the Ru particle-based electrocatalysts for Li-CO$_2$ cells, diverse sizes of particles were studied from two-digit nm to SACs. Li-CO$_2$ batteries with Ru SACs exhibited excellent electrochemical performance compared to those with larger Ru catalysts. The trend indicates that uniformly dispersed single atom-based catalysts can offer more catalytically active sites and maximize catalytic surface utilization [93].

Ir PARTICLE-BASED ELECTROCATALYSTS

Ir is a highly active noble metal-based catalyst used for electrochemical reactions, such as Li-O$_2$ batteries and water electrolysis [94-96]. Due to the high electrocatalytic activity, the Ir-based catalyst has recently begun to be applied to Li-CO$_2$ batteries [97]. To examine another example and emphasize the importance of size effects, the relationship between the size of Ir-based electrocatalysts and catalytic activities is reviewed in this chapter.

1. Morphology and Ir Particle Size Characterization

TEM images of various Ir particle-based electrocatalysts are presented to examine the structural characterization (Fig. 4). Mao et al. synthesized the IrO$_2$/MnO$_2$ catalyst material by using a hydrothermal method and the IrO$_2$/MnO$_2$ nanoflakes were uniformly grown on the carbon fibers of carbon cloth (Fig. 4(a)) [40]. The Ir nanoflakes had a thickness of about 5 nm, which is the largest case among the catalyst materials for comparison in Fig. 3. Ir/CNF as another case with a smaller Ir size loaded on CNF was reported (Fig. 4(b)) [98]. The CNFs were synthesized by subsequent heat treatment after electrospinning, and Ir nanoparticles with an average diameter of 3 nm were uniformly loaded on the CNFs after a series of thermal methods. Moreover, Gang et al. synthesized smaller Ir nanoparticles than IrO$_2$/MnO$_2$ and Ir/CNF, and Ir nanoparticles were loaded on N-doped CNT (N-CNT) (Fig. 4(c)) [99]. The N-CNTs were formed by spray pyrolysis chemical vapor deposition, and IrO$_2$ particles were dispersed on the N-CNTs by simply stirring and heating the Ir and N-CNT precursor solutions. The average size of the IrO$_2$ nanoparticles was 2.15 nm.

In addition to the Ir-based catalyst, our group previously conducted an in-depth study regarding the size effects of Ir catalysts on catalytic activity and electrochemical performance of Li-CO$_2$ cells. Rho et al. synthesized three different samples with diverse Ir
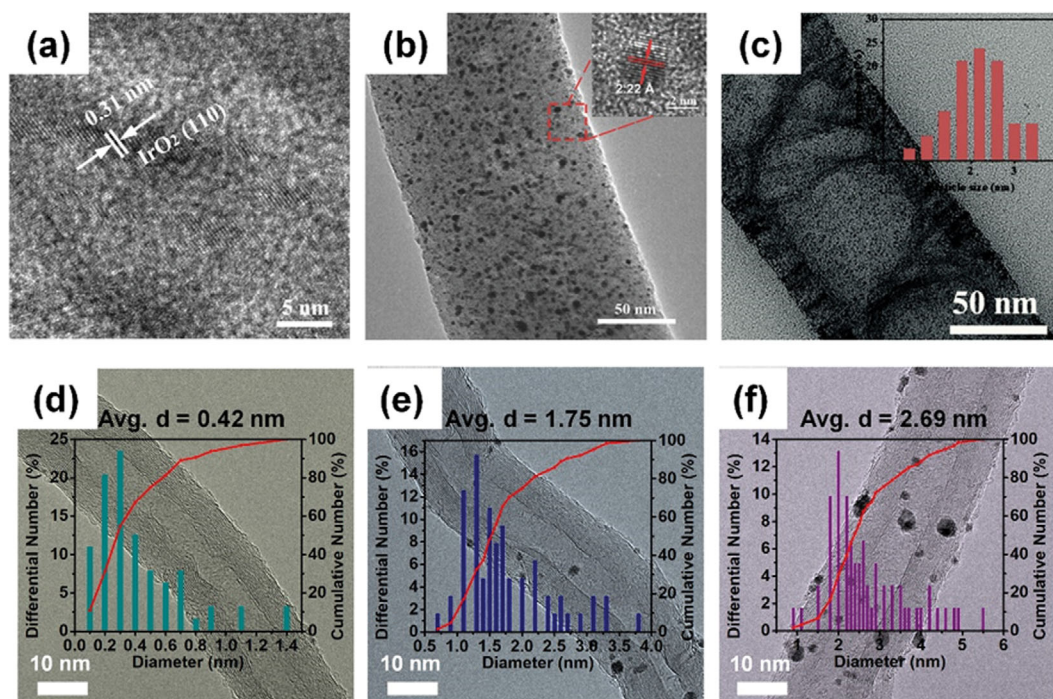
Fig. 4. TEM images of (a) IrO$_2$/MnO$_2$ (reproduced with permission from ref. [40], copyright 2019, Elsevier B.V.), (b) Ir/CNF (reproduced with permission from ref. [98], copyright 2018, John Wiley and Sons), (c) IrO$_2$/N-CNT (reproduced with permission from ref. [99], copyright 2020, Royal Society of Chemistry), (d) s-Ir/NCNT, (e) m-Ir/NCNT, and (f) l-Ir/NCNT (reproduced with permission from ref. [16], copyright 2022, Royal Society of Chemistry).

catalyst sizes loaded on to N-doped CNTs, called s-Ir/NCNT, m-Ir/NCNT, and l-Ir/NCNT (Fig. 4(d)-(f)) [16]. The amount and size of the Ir catalysts were successfully adjusted by controlling the amount of Ir precursor in the solution for synthesis. The average diameters of the Ir particles were 0.42, 1.75, and 2.69 nm, and the observable size distributions were 0.1-1.4, 0.7-3.8, and 0.9-5.5 nm for s-Ir/NCNT, m-Ir/NCNT, and l-Ir/NCNT, respectively. Based on the size distribution, it can be concluded that the values of the s-Ir/NCNT sample are close to those of SACs. While Ir nanoparticles of m-Ir/NCNT and l-Ir/NCNT are relatively non-uniformly loaded on the NCNTs, Ir atoms of s-Ir/NCNT exhibit uniform distribution on the NCNT supports.

2. Electrochemical Performance of Ir Particle-based Catalysts Embedded in Li-CO$_2$ Cells

To compare the electrocatalytic activity of diverse-sized Ir-based catalyst materials in Li-CO$_2$ batteries, discharge and charge curves are shown in Fig. 5(a)-(d). The Li-CO$_2$ cell employing IrO$_2$/MnO$_2$ with a catalyst size of 5 nm displays an overpotential of 1.4 V at 100 mA g^{-1} and discharge and charge voltages of 2.6 and 4.0 V, respectively (Fig. 5(a)) [40]. At the same current density, the full discharge capacity is 6,604 mAh g^{-1}. At 400 mA g^{-1}, the discharge capacity is maintained at 2,002 mAh g^{-1} after 80 cycles, and the cycle stability continues to 378 cycles with a limiting capacity of 1,000 mAh g^{-1}. The charge/discharge performance of Ir/CNF, which has a smaller Ir particle size (3 nm) than that of IrO$_2$/MnO$_2$, is displayed in Fig. 5(b) [98]. For the remaining stability for 45 cycles, the discharge and charge capacities are 21,528 and 20,045 mAh g^{-1}, respectively, at 50 mA g^{-1}, and the discharge platform is around

2.7 V. At a current density of 100 mA g^{-1}, the discharge and charge platforms indicate a 2.76 and 4.14 V resulting overpotential of 1.38 V, which is lower than that of IrO$_2$/MnO$_2$ (1.4 V). Furthermore, the discharge capacity is 18,813 mAh g^{-1} after 27 cycles at 100 mA g^{-1}. Compared to the capacity of 6,604 mAh g^{-1} from the IrO$_2$/MnO$_2$ catalyst with larger Ir particles, the Ir/CNF case shows much better catalytic activity and cell performance in Li-CO$_2$ batteries. The discharge/charge performance of the Li-CO$_2$ cell with IrO$_2$/N-CNT (average diameter of catalyst: 2.15 nm) is shown in Fig. 5(c) [99]. The discharge and charge plateaus are 2.61 and 3.95 V, respectively, at 100 mA g^{-1}; therefore, the overpotential is 1.34 V. This value is the smallest overpotential value among the other larger Ir particle-based catalysts mentioned above.

Our group attempted to examine the size effect of Ir SACs in Li-CO$_2$ batteries compared to that of larger Ir catalysts [16]. The discharge/charge performance of s-Ir/NCNT (SAC), m-Ir/NCNT (1.75 nm), and l-Ir/NCNT (2.69 nm) at 50 mA g^{-1} with a limit of 500 mAh g^{-1} after 15 cycles is shown in Fig. 5(d). When comparing the overpotential among the three catalysts, the degree of polarity is the highest in l-Ir/NCNT, showing the highest overpotential. The charge voltages decrease with a decrease in the Ir particle size: 4.5, 3.4, and 3.3 V for l-Ir/NCNT, m-Ir/NCNT, and s-Ir/NCNT, respectively. This tendency becomes more prominent as the cycle continues. The cycle-specific voltage gap between the discharge and charge reactions is shown in Fig. 5(e). After ten cycles, while the overpotential value rapidly increases for the l-Ir/NCNT, this rapidly decreases for the s-Ir/NCNT catalyst. This tendency implies that catalytic activity is activated in the case of Ir SACs during cycling.
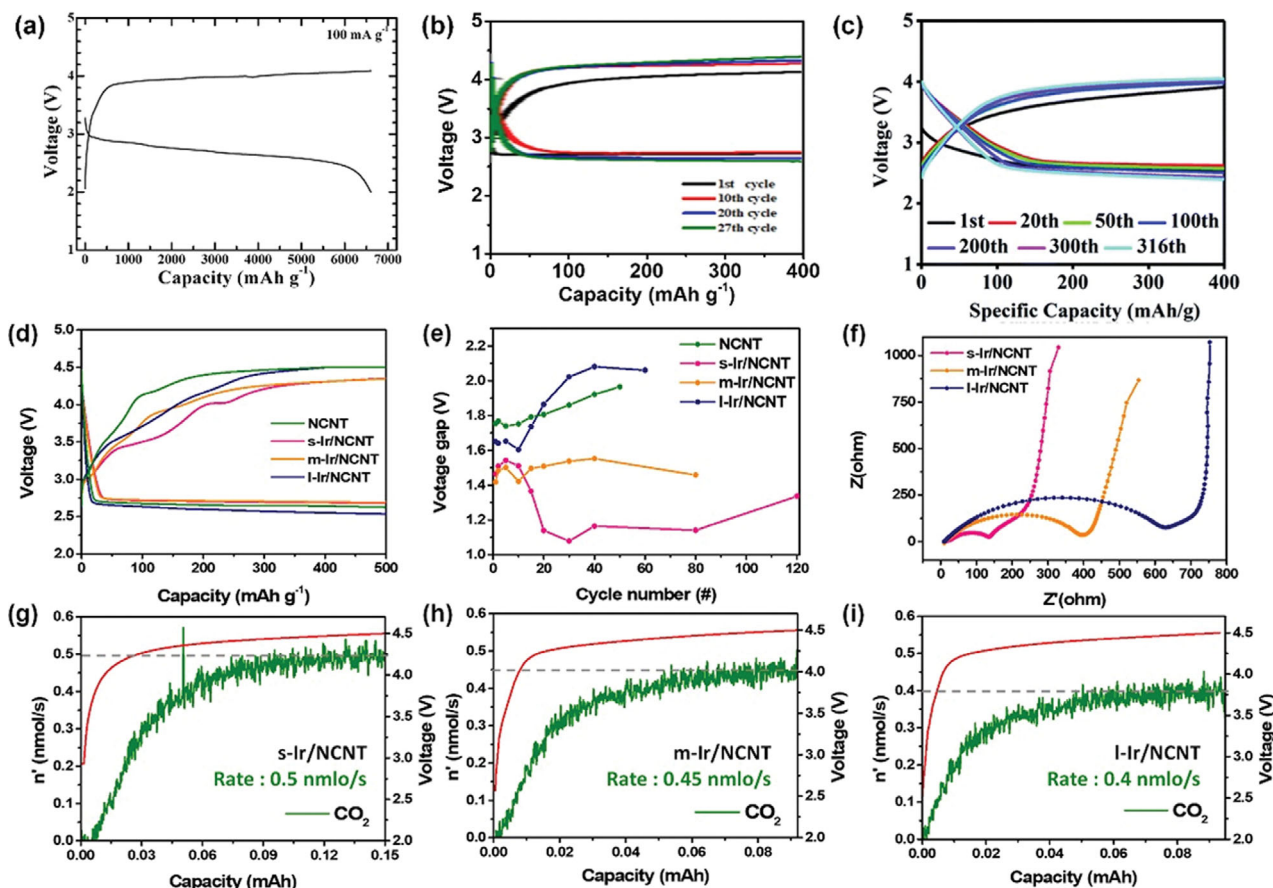
Fig. 5. Discharge/charge curves of (a) IrO₂/MnO₂ (reproduced with permission from ref. [40], copyright 2019, Elsevier B.V.), **(b)** Ir/CNF (reproduced with permission from ref. [98], copyright 2018, John Wiley and Sons), **(c)** IrO₂/N-CNT (reproduced with permission from ref. [99], copyright 2020, Royal Society of Chemistry), **(d)** s-Ir/NCNT, m-Ir/NCNT, and l-Ir/NCNT. **(e)** Voltage gap graphs calculated during discharging and charging, **(f)** EIS profiles after ten cycles, and **(g)-(i)** *in-situ* DEMS results for the gas evolution rate of CO₂ during the charge reaction of s-Ir/NCNT, m-Ir/NCNT, and l-Ir/NCNT (reproduced with permission from ref. [16], copyright 2022, Royal Society of Chemistry).

The overpotential of s-Ir/NCNT shows an impressive value of 1.07 V after the 30th cycle, which is the lowest value among the Ir particle-based catalysts referred to above. The s-Ir/NCNT delivers excellent cycle performance exceeding 120 cycles, while the m-Ir/NCNT and l-Ir/NCNT are degraded after 80 and 60 cycles, respectively. To examine the surface resistance, the electrochemical impedance spectroscopy measurements of the s-Ir/NCNT, m-Ir/NCNT, and l-Ir/NCNT are shown in Fig. 5(f). The charge-transfer resistance, which is shown as the diameter of a semicircle between the electrode and electrolyte surface, is about 400 and 650 Ω for the m-Ir/NCNT and l-Ir/NCNT, respectively. On the other hand, the s-Ir/NCNT shows a decreased charge-transfer resistance value of 150 Ω This result demonstrates that the Li-CO₂ reaction is successfully facilitated with reduced resistance by employing SACs (s-Ir/NCNT). To confirm that the facile Li₂CO₃ decomposition reaction occurs while charging, *in-situ* differential electrochemical mass spectrometry (DEMS) results are displayed (Fig. 5(g)-(i)). During the recharge process, CO₂ gas is released by the reverse decomposition of Li₂CO₃. Therefore, the CO₂ evolution rate analyzed by DEMS demonstrates the degree of reversibility in the Li-CO₂ reaction. The CO₂ evolution shows the highest rate for the s-Ir/NCNT

(0.5 nmol s⁻¹) compared to that for the m-Ir/NCNT (0.45 nmol s⁻¹) and l-Ir/NCNT (0.4 nmol s⁻¹). This reveals that the s-Ir/NCNT catalyst with atomically minimized catalyst size offers excellent catalytic activity and superior reversibility.

To elucidate the reaction pathway and excellent activity of SACs, the result of calculating the reaction energy (ΔG) through simulation is shown in Fig. 6. First, the most preferred calculated Li-CO₂ reaction pathway goes through nine intermediates. In the discharge reaction, Li₂CO₃ and C are generated by first forming a LiCO₂ intermediate from Li and then binding to Li again; thus, the reaction proceeds stably. This pathway becomes a spontaneous reaction where ΔG is lowered. When charging, an additional potential corresponding to the ΔG is given to create a spontaneous pathway, meaning additional cell voltage is required. In the case of s-Ir/NCNT, it is necessary to additionally apply an overpotential of 1.53 V to return to the original state including Li and CO₂ after the discharging process to make the charging process reversible (Fig. 6(a)). On the other hand, when the particle increases in size, the overpotential increases; thus, it is calculated that the reverse reaction with Li and CO₂ occurs only when an overpotential of 4.92 V for nanoparticles and 5.26 V for bulk Ir is added. Therefore, it can be seen from
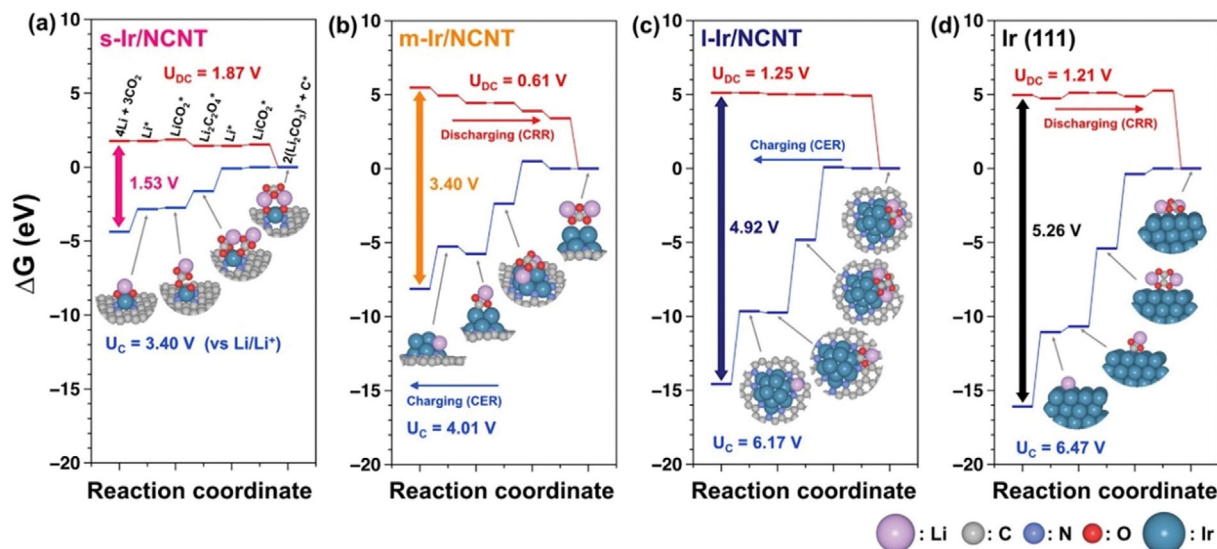
Fig. 6. Discharge/charge reaction energy diagram of a Li-CO$_2$ battery for (a) s-Ir/NCNT, (b) m-Ir/NCNT, (c) l-Ir/NCNT, and (d) Ir (111) surfaces (reproduced with permission from ref. [16], copyright 2022, Royal Society of Chemistry).

the previous experimental results in Fig. 5(d)-(i) and calculation results in Fig. 6 that atomizing the Ir metal can successfully reduce overpotential.

In summary, there have been several studies for Ir particle-based catalysts in Li-CO$_2$ batteries and diverse sizes of Ir particles are synthesized from 5 nm to a single atom unit. The overpotential in the discharge and charge reaction decreases with decreasing catalyst particle size, which means that the atomical miniaturization of catalysts can not only effectively facilitate the Li-CO$_2$ reaction, but also reduce expensive noble metal components in catalyst materials. The density functional theory (DFT) calculation results also support the high reversibility in SAC-applied batteries.

SAC CANDIDATES FOR NEXT-GENERATION Li-CO$_2$ BATTERIES

The excellent catalytic effect of SACs can further maximize the electrochemical performance for Li-CO$_2$ batteries. Considerable efforts have been made to homogeneously and stably load SAC particles using the facile synthesis method [100]. This section of the review introduces other possible candidates for precious metal-based SACs employing diverse support materials that are potentially suitable for Li-CO$_2$ batteries.

Wan et al. made defects on TiO$_2$ nanosheets to act as an optimal support material of Au atoms (Au/TiO$_2$) [101]. TiO$_2$ nanosheets are formed through a series of heat treatments of the precursor gel. Then, some defects are formed in TiO$_2$ nanosheets by calcinating them in a reducing atmosphere. In this process, oxygen vacancies are generated in TiO$_2$. For the last step, Au atoms are loaded on to the TiO$_2$ nanosheets through stirring and calcination of Au and TiO$_2$ nanosheet precursors, constructing a Ti-Au-Ti structure. The valuable characteristic of this catalyst is that the defect of TiO$_2$ forms strong binding between Au atom metals and the TiO$_2$ supports, resulting in catalytic stability and high activity. TEM images of Au/TiO$_2$ demonstrate that the SACs are successfully synthe-

sized (Fig. 7(a)). Furthermore, the conversion of CO through the DFT calculation shows higher catalytic activity at the Au single atom compared to the Au (111) surface. By manipulating this kind of Au-based SAC, boosted catalytic activity and performance can be expected for the Li-CO$_2$ reaction. The defect engineering of support material can generate oxygen vacancy, which can be a binding site of single atom metals and a promising reaction site [59,60,73].

Liu et al. suggested that MCM-22 serves as a framework in which Pt atomic catalysts exist (Pt/MCM-22) [102]. As seen in Fig. 7(b), the pure siliceous layered precursor of MCM-22 (MWW zeolite precursor, MWW(P)) is expanded by introducing hexadecyltrimethylammonium (CTMA$^+$OH$^-$) at the swelling process. After, Pt atoms enter the expanded gaps of MWW and are fixed by thermal treatment. By encapsulating the Pt atoms, the structure of MCM-22 serves as the stable supporter for Pt SACs. The TEM images show that the Pt atoms are highly dispersed and stably anchored on the MCM-22 framework (Fig. 7(b)). Furthermore, a high-temperature stability test was conducted for Pt/MCM-22. Even under the harsh conditions of oxygen and reduction treatment at 650 °C, this Pt/MCM-22 material successfully exhibits high stability. Therefore, the complex zeolite structure with highly well-anchored single atoms could be another catalyst alternative for stably working Li-CO$_2$ batteries.

In addition to Pt/MCM-22, there is another case wherein Pt SACs are applied to Li-O$_2$ batteries. Zhao et al. used holey ultrathin g-C$_3$N$_4$ nanosheets for Pt support and employed them as a cathode for a Li-O$_2$ battery (Pt/CNHS) [55]. Bulk g-C$_3$N$_4$ (CNB) is formed through thermal polycondensation of melamine, then holey g-C$_3$N$_4$ nanosheets (CNHS) are synthesized via the two-step calcination of CNB. After adding Pt precursor solution and further heat treatments, Pt atoms are successfully loaded on to CNHS supports through a liquid phase reaction (Fig. 7(c)). The TEM image shows the nanosheet substrates with pores and dispersed Pt atoms. Li-O$_2$ cells employing the Pt/CNHS show superior catalytic performance with low overpotential and improved cycle performance. This is
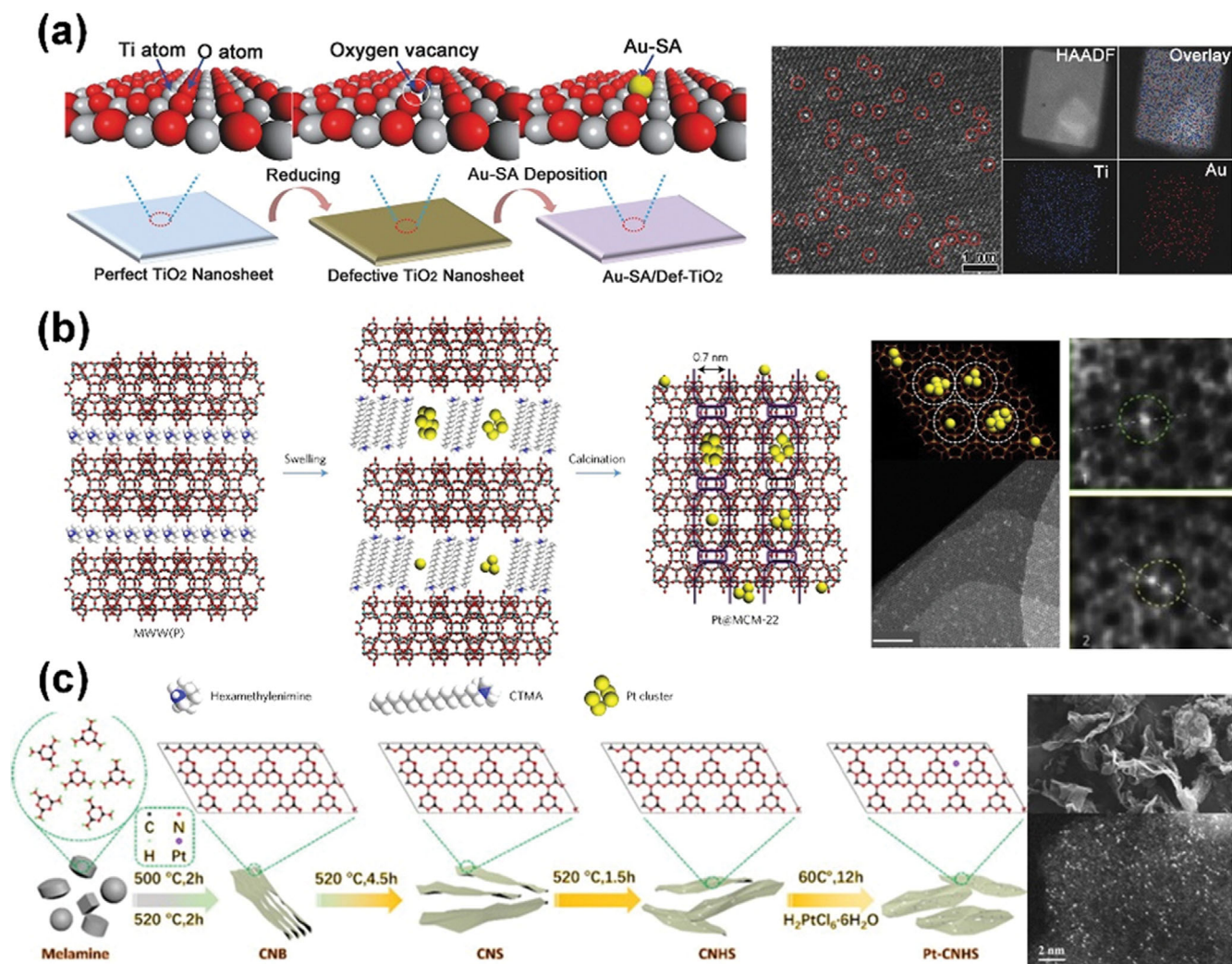
Fig. 7. SAC candidates for Li-CO$_2$ batteries: Schematic illustration of the synthesis procedure and TEM images of (a) Au/TiO$_2$ (reproduced with permission from ref. [101], copyright 2018, John Wiley and Sons), (b) Pt/MCM-22 (reproduced with permission from ref. [104], copyright 2018, American Chemical Society), and (c) Pt/CNHS (reproduced with permission from ref. [55], copyright 2020, Elsevier).

due primarily to the edge sites created by the hole not only creating a place for Pt atoms to be stably dispersed, but also providing an active catalytic site. Furthermore, this porous structure provides a large surface area, facilitating speedy mass transport and providing more space to accommodate Li$_2$O$_2$ discharge product. Pt single atoms with high electrical conductivity can supply effective mass transfer and stable reaction sites during the Li-O$_2$ reaction. Therefore, this type of catalyst could also be a promising candidate for high performance Li-CO$_2$ cells.

In addition to the synthetic methods we mentioned above, a plasma etching method for a practical material process has recently been studied by Peng et al. [103], who used nanocarbon (NC) for metal supports. For plasma-enhanced chemical vapor deposition (PECVD) process under N$_2$ flow, abundant defects are generated on the NC supports. Metal atoms such as Fe, Co, and Ni are preferentially trapped in the defected NC. The PECVD strategy is highly efficient for large-scale production of SAC based materials, so that we can easily scale up to gram level. We expect that devel-

oping the facile and versatile way to fabricate SACs would give a vision of enabling practical application of the SACs in a large area, including Li-CO$_2$ battery field.

Various methods for synthesizing the SACs have been attempted for various applications. The studies mentioned above not only focused on simple and scale-up synthesis, but also tried to achieve the stable and homogeneous distribution of metal atom catalysts. These studies proposed diverse strategies for modifying support materials for SACs, such as the generation of oxygen defects, introduction of porous materials, and artificial pore generation. In addition, the studies regarding practical method for large-scale synthesis would suggest a way to get closer to commercializing SACs.

CONCLUSION

This review highlights catalyst size miniaturization of noble metal-based electrocatalysts from nanoparticle to single atom units for high performance Li-CO$_2$ cells. Previous studies controlled the

size of noble metal particles through various facile synthesis methods with diverse supports. Among the noble metals, Ru- and Ir-based catalysts have commonly been studied for Li-CO_2 batteries. Among various Ru and Ir particle-based catalysts, the atomically loaded catalysts display the lowest discharge/charge overpotential in Li-CO_2 cells compared to others with larger particle sizes. DFT calculation for reaction energy also demonstrates that the lowest overvoltage can be achieved by using SACs. Besides the catalysts above, although it has not yet been applied as a Li-CO_2 battery, it is possible that there are many SAC candidates that exhibit sufficiently high catalytic activity. To enable further breakthrough in Li-CO_2 technology and its realization in the practical aspect, utilization of atomic noble metal catalysts is the most promising strategy.

ACKNOWLEDGEMENTS

REFERENCES

1. D. Davies, M. Verde, O. Mnyshenko, Y. Chen, R. Rajeev, Y. Meng and G. Elliott, *Nat. Energy*, **4**, 42 (2019).
2. L. Zhang, Z. J. Zhao and J. Gong, *Angew. Chem. Int. Ed.*, **56**, 11326 (2017).
3. J.-R. Youn, M.-J. Kim, S.-J. Lee, I.-S. Ryu, S. K. Jeong, K. Lee and S. G. Jeon, *Korean J. Chem. Eng.*, **39**, 2334 (2022).
4. Y. Jia-xi, G. Dan, Q. You-wei and Z. Heng, *Korean J. Chem. Eng.*, **39**, 2010 (2022).
5. J. H. Jeong, S. Kim, M.-J. Park and W. B. Lee, *Korean J. Chem. Eng.*, **39**, 1709 (2022).
6. N. MacDowell, N. Florin, A. Buchard, J. Hallett, A. Galindo, G. Jackson, C. S. Adjiman, C. K. Williams, N. Shah and P. Fennell, *Energy Environ. Sci.*, **3**, 1645 (2010).
7. A. Mustafa, B. G. Lougou, Y. Shuai, S. Razzaq, Z. Wang, E. Shagdar and J. Zhao, *J. Electrochem. Sci. Technol.*, **13**, 148 (2022).
8. B. J. Kim and S. W. Kang, *Korean J. Chem. Eng.*, **39**, 2542 (2022).
9. H. Yamada, *Polym. J.*, **53**, 93 (2021).
10. E. A. Parson and D. W. Keith, *Science*, **282**, 1053 (1998).
11. S. Kim and D. H. Jeong, *Korean J. Chem. Eng.*, **39**, 1999 (2022).
12. J.-H. Kang, J. Lee, J.-W. Jung, J. Park, T. Jang, H.-S. Kim, J.-S. Nam, H. Lim, K. R. Yoon and W.-H. Ryu, *ACS Nano*, **14**, 14549 (2020).
13. Y. Qiao, J. Yi, S. Wu, Y. Liu, S. Yang, P. He and H. Zhou, *Joule*, **1**, 359 (2017).
14. J.-Y. Lee, H.-S. Kim, J.-S. Lee, C.-J. Park and W.-H. Ryu, *ACS Sust. Chem. Eng.*, **7**, 16151 (2019).
15. H.-S. Kim, J.-Y. Lee, J.-K. Yoo and W.-H. Ryu, *ACS Mater. Lett.*, **3**, 815 (2021).
16. Y.-J. Rho, B. Kim, K. Shin, G. Henkelman and W.-H. Ryu, *J. Mater. Chem. A*, **10**, 19710 (2022).
17. S. Xu, S. K. Das and L. A. Archer, *RSC Adv.*, **3**, 6656 (2013).
18. L. Wang, W. Dai, L. Ma, L. Gong, Z. Lyu, Y. Zhou, J. Liu, M. Lin, M. Lai and Z. Peng, *ACS Omega*, **2**, 9280 (2017).
19. H. Liang, Y. Zhang, F. Chen, S. Jing, S. Yin and P. Tsiakaras, *Appl. Catal. B: Environ.*, **244**, 559 (2019).
20. Y. Jiao, J. Qin, H. M. K. Sari, D. Li, X. Li and X. Sun, *Energy Storage Mater.*, **34**, 148 (2021).
21. X. Hu, Z. Li and J. Chen, *Angew. Chem.*, **129**, 5879 (2017).
22. Z. Zhang, Q. Zhang, Y. Chen, J. Bao, X. Zhou, Z. Xie, J. Wei and Z. Zhou, *Angew. Chem.*, **127**, 6650 (2015).
23. X. Zhang, Q. Zhang, Z. Zhang, Y. Chen, Z. Xie, J. Wei and Z. Zhou, *Chem. Commun.*, **51**, 14636 (2015).
24. Y. Liu, R. Wang, Y. Lyu, H. Li and L. Chen, *Energy Environ. Sci.*, **7**, 677 (2014).
25. X. Li, S. Yang, N. Feng, P. He and H. Zhou, *Chin. J. Catal.*, **37**, 1016 (2016).
26. Z. Zhao, J. Huang and Z. Peng, *Angew. Chem. Int. Ed.*, **57**, 3874 (2018).
27. S. R. Gowda, A. Brunet, G. Wallraff and B. D. McCloskey, *J. Phys. Chem. Lett.*, **4**, 276 (2013).
28. H.-K. Lim, H.-D. Lim, K.-Y. Park, D.-H. Seo, H. Gwon, J. Hong, W. A. Goddard III, H. Kim and K. Kang, *J. Am. Chem. Soc.*, **135**, 9733 (2013).
29. C. Ling, R. Zhang, K. Takechi and F. Mizuno, *J. Phys. Chem. C*, **118**, 26591 (2014).
30. M.-K. Song, S. Park, F. M. Alamgir, J. Cho and M. Liu, *Mater. Sci. Eng.: R: Rep.*, **72**, 203 (2011).
31. A. Ahmadiparidari, R. E. Warburton, L. Majidi, M. Asadi, A. Chamaani, J. R. Jokisaari, S. Rastegar, Z. Hemmat, B. Sayahpour and R. S. Assary, *Adv. Mater.*, **31**, 1902518 (2019).
32. B. C. Kwon, N.-K. Park, M. Kang, D. Kang, M. W. Seo, D. Lee, S. G. Jeon and H.-J. Ryu, *Korean J. Chem. Eng.*, **38**, 1188 (2021).
33. Y. Hou, J. Wang, L. Liu, Y. Liu, S. Chou, D. Shi, H. Liu, Y. Wu, W. Zhang and J. Chen, *Adv. Funct. Mater.*, **27**, 1700564 (2017).
34. A. Hu, C. Shu, C. Xu, R. Liang, J. Li, R. Zheng, M. Li and J. Long, *J. Mater. Chem. A*, **7**, 21605 (2019).
35. R. Pipes, A. Bhargav and A. Manthiram, *ACS Appl. Mater. Interfaces*, **10**, 37119 (2018).
36. Z. Zhang, Z. Zhang, P. Liu, Y. Xie, K. Cao and Z. Zhou, *J. Mater. Chem. A*, **6**, 3218 (2018).
37. Z. Zhang, W.-L. Bai, K.-X. Wang and J.-S. Chen, *Energy Environ. Sci.*, **13**, 4717 (2020).
38. A. Suryatna, I. Raya, L. Thangavelu, F. R. Alhachami, M. M. Kadhim, U. S. Altimari, Z. H. Mahmoud, Y. F. Mustafa and E. Kianfar, *J. Chem.*, **2022**, 1 (2022).
39. M. Rahman, X. Wang and C. Wen, *J. Appl. Electrochem.*, **44**, 5 (2014).
40. Y. Mao, C. Tang, Z. Tang, J. Xie, Z. Chen, J. Tu, G. Cao and X. Zhao, *Energy Storage Mater.*, **18**, 405 (2019).
41. Y. Qiao, S. Xu, Y. Liu, J. Dai, H. Xie, Y. Yao, X. Mu, C. Chen, D. J. Kline and E. M. Hitz, *Energy Environ. Sci.*, **12**, 1100 (2019).
42. J.-J. Xu, Z.-L. Wang, D. Xu, L.-L. Zhang and X.-B. Zhang, *Nat. Commun.*, **4**, 1 (2013).
43. C. Zhao, C. Yu, M. N. Banis, Q. Sun, M. Zhang, X. Li, Y. Liu, Y. Zhao, H. Huang and S. Li, *Nano Energy*, **34**, 399 (2017).
44. D. Su, D. Han Seo, Y. Ju, Z. Han, K. Ostrikov, S. Dou, H.-J. Ahn, Z. Peng and G. Wang, *NPG Asia Mater.*, **8**, e286 (2016).
45. B. Sun, X. Huang, S. Chen, P. Munroe and G. Wang, *Nano Lett.*,

14, 3145 (2014).

46. B. Sun, S. Chen, H. Liu and G. Wang, *Adv. Funct. Mater.*, **25**, 4436 (2015).

47. Q. Shi, C. Zhu, D. Du and Y. Lin, *Chem. Soc. Rev.*, **48**, 3181 (2019).

48. J. Kim, H. E. Kim and H. Lee, *ChemSusChem*, **11**, 104 (2018).

49. J.-g. Choi, K. Ham, S. Bong and J. Lee, *J. Electrochem. Sci. Technol.*, **13**, 354 (2022).

50. J. Lu, Y. Jung Lee, X. Luo, K. Chun Lau, M. Asadi, H.-H. Wang, S. Brombosz, J. Wen, D. Zhai and Z. Chen, *Nature*, **529**, 377 (2016).

51. C. Shu, C. Wu, J. Long, H. Guo, S.-X. Dou and J. Wang, *Nano Energy*, **57**, 166 (2019).

52. T. Liu, Z. Liu, G. Kim, J. T. Frith, N. Garcia-Araez and C. P. Grey, *Angew. Chem.*, **129**, 16273 (2017).

53. B. Qiao, A. Wang, X. Yang, L. F. Allard, Z. Jiang, Y. Cui, J. Liu, J. Li and T. Zhang, *Nat. Chem.*, **3**, 634 (2011).

54. F. Chen, G. Zhang, Y. Zhang, S. Cao and J. Li, *J. Electrochem. Sci. Technol.*, **13**, 362 (2022).

55. W. Zhao, J. Wang, R. Yin, B. Li, X. Huang, L. Zhao and L. Qian, *J. Colloid Interface Sci.*, **564**, 28 (2020).

56. J. Long, Z. Hou, C. Shu, C. Han, W. Li, R. Huang and J. Wang, *ACS Appl. Mater. Interfaces*, **11**, 3834 (2019).

57. H. Wang, H. Wang, J. Huang, X. Zhou, Q. Wu, Z. Luo and F. Wang, *ACS Appl. Mater. Interfaces*, **11**, 44556 (2019).

58. W. Zhao, X. Li, R. Yin, L. Qian, X. Huang, H. Liu, J. Zhang, J. Wang, T. Ding and Z. Guo, *Nanoscale*, **11**, 50 (2019).

59. J.-W. Jung, G.-Y. Kim, N.-W. Lee and W.-H. Ryu, *Appl. Surf. Sci.*, **533**, 147496 (2020).

60. N.-W. Lee, K. R. Yoon, J.-Y. Lee, Y. Park, S.-J. Pyo, G.-Y. Kim, D.-H. Ha and W.-H. Ryu, *ACS Appl. Energy Mater.*, **2**, 3513 (2019).

61. S. Kim, J. Park, J. Hwang and J. Lee, *EnergyChem*, **3**, 100054 (2021).

62. T. Chao, Y. Hu, X. Hong and Y. Li, *ChemElectroChem*, **6**, 289 (2019).

63. H. Lee, Y. J. Kim, Y. Sohn and C. K. Rhee, *J. Electrochem. Sci. Technol.*, **12**, 323 (2021).

64. J. Jana, Y.-L. T. Ngo, J. S. Chung and S. H. Hur, *J. Electrochem. Sci. Technol.*, **11**, 220 (2020).

65. H. S. Kim, B. Kim, H. Park, J. Kim and W. H. Ryu, *Adv. Energy Mater.*, **12**, 2103527 (2022).

66. G.-Y. Kim, J. Lee, Y.-J. Rho, W.-H. Kim, M. Kim, J.-H. Ahn and W.-H. Ryu, *Chem. Eng. J.*, **446**, 136951 (2022).

67. W.-H. Ryu, F. S. Gittleson, J. M. Thomsen, J. Li, M. J. Schwab, G. W. Brudvig and A. D. Taylor, *Nat. Commun.*, **7**, 1 (2016).

68. B. E. Hayden, *Accounts Chem. Res.*, **46**, 1858 (2013).

69. M. Shao, A. Peles and K. Shoemaker, *Nano Lett.*, **11**, 3714 (2011).

70. S. Mukerjee, *J. Appl. Electrochem.*, **20**, 537 (1990).

71. J. Hwang, *Korean J. Chem. Eng.*, **38**, 1104 (2021).

72. G. Zheng, J. Yin, Z. Guo, S. Tian and X. Yang, *J. Electrochem. Sci. Technol.*, **12**, 458 (2021).

73. G. Y. Kim, K. R. Yoon, K. Shin, J. W. Jung, G. Henkelman and W. H. Ryu, *Small*, **17**, 2103755 (2021).

74. Q. Zhang and J. Guan, *Adv. Funct. Mater.*, **30**, 2000768 (2020).

75. N. Cheng, L. Zhang, K. Doyle-Davis and X. Sun, *Electrochem. Energy Rev.*, **2**, 539 (2019).

76. C. X. Zhao, B. Q. Li, J. N. Liu and Q. Zhang, *Angew. Chem. Int. Ed.*, **60**, 4448 (2021).

77. A. Wang, J. Li and T. Zhang, *Nat. Rev. Chem.*, **2**, 65 (2018).

78. L. Zhang, Y. Ren, W. Liu, A. Wang and T. Zhang, *National Sci. Rev.*, **5**, 653 (2018).

79. X.-F. Yang, A. Wang, B. Qiao, J. Li, J. Liu and T. Zhang, *Accounts Chem. Res.*, **46**, 1740 (2013).

80. S. Lin, C. S. Diercks, Y.-B. Zhang, N. Kornienko, E. M. Nichols, Y. Zhao, A. R. Paris, D. Kim, P. Yang and O. M. Yaghi, *Science*, **349**, 1208 (2015).

81. X. Zhang, Z. Wu, X. Zhang, L. Li, Y. Li, H. Xu, X. Li, X. Yu, Z. Zhang and Y. Liang, *Nat. Commun.*, **8**, 1 (2017).

82. H. Zhang, G. Liu, L. Shi and J. Ye, *Adv. Energy Mater.*, **8**, 1701343 (2018).

83. R. Qin, P. Liu, G. Fu and N. Zheng, *Small Methods*, **2**, 1700286 (2018).

84. X. Guo, P. Liu, J. Han, Y. Ito, A. Hirata, T. Fujita and M. Chen, *Adv. Mater.*, **27**, 6137 (2015).

85. F. Li, D. M. Tang, T. Zhang, K. Liao, P. He, D. Golberg, A. Yamada and H. Zhou, *Adv. Energy Mater.*, **5**, 1500294 (2015).

86. Y.-C. Lu, H. A. Gasteiger and Y. Shao-Horn, *J. Am. Chem. Soc.*, **133**, 19048 (2011).

87. C. A. Huff and M. S. Sanford, *ACS Catal.*, **3**, 2412 (2013).

88. S. Yang, Y. Qiao, P. He, Y. Liu, Z. Cheng, J.-j. Zhu and H. Zhou, *Energy Environ. Sci.*, **10**, 972 (2017).

89. Y. Qiao, J. Wu, J. Zhao, Q. Li, P. Zhang, C. Hao, X. Liu, S. Yang and Y. Liu, *Energy Storage Mater.*, **27**, 133 (2020).

90. S. Bie, M. Du, W. He, H. Zhang, Z. Yu, J. Liu, M. Liu, W. Yan, L. Zhou and Z. Zou, *ACS Appl. Mater. Interfaces*, **11**, 5146 (2019).

91. Z. Lian, Y. Lu, C. Wang, X. Zhu, S. Ma, Z. Li, Q. Liu and S. Zang, *Adv. Sci.*, **8**, 2102550 (2021).

92. J. Lin, J. Ding, H. Wang, X. Yang, X. Zheng, Z. Huang, W. Song, J. Ding, X. Han and W. Hu, *Adv. Mater.*, **34**, 2200559 (2022).

93. B. Lu, Q. Liu and S. Chen, *ACS Catal.*, **10**, 7584 (2020).

94. G. Liu, J. Xu, Y. Wang and X. Wang, *J. Mater. Chem. A*, **3**, 20791 (2015).

95. K. Guo, Y. Li, T. Yuan, X. Dong, X. Li and H. Yang, *J. Solid State Electrochem.*, **19**, 821 (2015).

96. W. Zhou, Y. Cheng, X. Yang, B. Wu, H. Nie, H. Zhang and H. Zhang, *J. Mater. Chem. A*, **3**, 14556 (2015).

97. Y. Xing, Y. Yang, D. Li, M. Luo, N. Chen, Y. Ye, J. Qian, L. Li, D. Yang and F. Wu, *Adv. Mater.*, **30**, 1803124 (2018).

98. C. Wang, Q. Zhang, X. Zhang, X. G. Wang, Z. Xie and Z. Zhou, *Small*, **14**, 1800641 (2018).

99. G. Wu, X. Li, Z. Zhang, P. Dong, M. Xu, H. Peng, X. Zeng, Y. Zhang and S. Liao, *J. Mater. Chem. A*, **8**, 3763 (2020).

100. H. Tian, A. Song, H. Tian, J. Liu, G. Shao, H. Liu and G. Wang, *Chem. Sci.*, **12**, 7656 (2021).

101. J. Wan, W. Chen, C. Jia, L. Zheng, J. Dong, X. Zheng, Y. Wang, W. Yan, C. Chen and Q. Peng, *Adv. Mater.*, **30**, 1705369 (2018).

102. L. Liu, U. Diaz, R. Arenal, G. Agostini, P. Concepcion and A. Corma, *Nat. Mater.*, **16**, 132 (2017).

103. P. Rao, D. Wu, Y.-Y. Qin, J. Luo, J. Li, C. Jia, P. Deng, W. Huang, Y. Su and Y. Shen, *J. Mater. Chem. A*, **10**, 6531 (2022).

104. L. Liu and A. Corma, *Chem. Rev.*, **118**, 4981 (2018).

Prof. Won-Hee Ryu received his BS (2006) from department of metallurgical engineering at Yonsei University, Korea and MS (2007) & PhD (2012) from department of materials science and engineering at Korea Advanced Institute of Science and Technology (KAIST), Korea. During his PhD course, he worked as a visiting researcher in the electrochemical energy storage department at the Argonne National Laboratory, USA. Prof. Ryu did postdoctoral works at KAIST (2012-2013) and Yale University (2013-2016). He joined the faculty of the department of chemical and biological engineering at Sookmyung Women's University (Seoul, Korea) as an assistant professor (2016) and currently work as an associate professor from 2021. Prof. Ryu has published more than 75 papers and 34 international and domestic patents. He has been recognized with several fellowship and awards including The NatureNet Science Fellows (2014-2016), The Korean Electrochemical Society (KECS) Park Sumun Award (2022), and Journal of Materials Chemistry A Emerging Investigators (2022).